

Weyl superconductivity and quasiperiodic Majorana arcs in quasicrystals

Masahiro Hori,^{1,2,*} Ryo Okugawa,² K. Tanaka,¹ and Takami Tohyama²

¹*Department of Physics and Engineering Physics,
and Centre for Quantum Topology and Its Applications (quanTA),
University of Saskatchewan, 116 Science Place, Saskatoon, Saskatchewan, Canada S7N 5E2*

²*Department of Applied Physics, Tokyo University of Science, Tokyo 125-8585, Japan*

(Dated: March 15, 2024)

Weyl superconductivity is a topological phase in three-dimensional crystals in which the Weyl equation describes quasiparticle excitation near band-touching points in momentum space called Weyl nodes. For quasicrystals which lack translational symmetry, a theory of Weyl superconductivity has not been established, in spite of recent extensive studies on quasicrystalline topological phases. Here, we demonstrate the occurrence of quasicrystalline Weyl superconductivity by extending the definition of Weyl superconductivity to periodically stacked, two-dimensional superconducting quasicrystals. We identify quasicrystalline Weyl nodes – topologically protected point nodes in one-dimensional momentum space corresponding to the stacking direction – in terms of a topological invariant given by a change in the Bott index in quasicrystalline layers. We find that these Weyl nodes exist in pairs and that Majorana zero-energy modes protected by the nonzero Bott index between a pair of quasicrystalline Weyl nodes appear on surfaces. These Majorana zero modes form an infinite number of arcs in momentum space, densely and quasiperiodically distributed as a function of momentum in the direction of surfaces within each quasicrystalline layer. In Ammann-Beenker (Penrose) quasicrystals, the quasiperiodicity of Majorana arcs is governed by the silver (golden) ratio associated with the quasicrystalline structure.

I. INTRODUCTION

Quasicrystals (QCs) are materials whose structure is aperiodic with a long-range order [1]. Recent experiments in QCs have shown the presence of electronic long-range orders, similarly to crystals, such as a long-range magnetic order [2] and superconductivity [3, 4]. On the other hand, it has been shown theoretically that quasicrystalline superconductors exhibit Cooper pairs with finite center-of-mass momentum [5–8] and anomalous paramagnetic response [9], which are different from crystalline superconductors. Furthermore, some theoretical works have predicted topological phases in QCs without crystalline counterparts [10].

One cannot use a topological band theory for QCs because they lack translational symmetry. Nevertheless, in quasicrystalline systems, topological insulator phases beyond a topological band theory [11–20], topological charge pumping [21–25], and topological semimetals [26–32] have been proposed theoretically. In particular, layered QCs have attracted attention recently as a platform for realizing topological semimetallic phases [29–32].

Some crystalline topological superconductors show gapless points in momentum space called point nodes. If those points cannot be gapped out by weak perturbations that conserve symmetries of the system, such points are called topologically protected nodes. For example, a Weyl superconductor (WSC) is a three-dimensional (3D) superconductor with topologically protected point nodes called Weyl nodes, which exist pairwise and are described by the Weyl equation with chirality ± 1 [33–42]. In 3D

momentum space, the Chern number changes at each Weyl node by its chirality [43–45]. WSCs also have zero-energy surface states protected by the nonzero Chern number between a pair of Weyl nodes [46]. Those zero-energy modes are localized at the surfaces and form arcs in momentum space. These arcs are called Majorana arcs because zero-energy modes in topological superconductors can be described as Majorana fermions [47]. Also in QCs, some theoretical works [48–51] including studies by some of the present authors [52, 53] have proposed topological superconductivity with no node. Whether a quasicrystalline topological superconductor with nodes can exist or not has yet to be understood because the nodes generally appear in the Brillouin zone of periodic systems.

In this work, we study periodically stacked, two-dimensional (2D) quasicrystalline topological superconductors. We find that this system shows topologically protected nodes in one-dimensional momentum space corresponding to the stacking direction. At these nodes, the Bott index changes its value in the same way as does the Chern number at Weyl nodes in crystalline WSCs. We thus call them quasicrystalline Weyl nodes [30] and the resulting superconductors quasicrystalline WSCs. Between two of such quasicrystalline Weyl nodes in momentum space, zero-energy modes protected by the nonzero Bott index appear on surfaces. Fourier momenta at which the Fourier amplitudes of these zero-energy surface modes are finite are densely and quasiperiodically distributed in one-dimensional momentum space that corresponds to the direction of surfaces within each layer. This quasiperiodic distribution of momenta of the motion along each surface in 2D QCs is in stark contrast to periodic distribution due to repeating Brillouin zones

* mhori@japan@gmail.com

of layered 2D crystalline topological superconductors.

The paper is organized as follows. We first review a 2D quasicrystalline topological superconductor in Sec. II A and then introduce a layered quasicrystalline superconductor in Sec. II B. In Sec. III A, we extend the definition of Weyl superconductivity in crystals to QCs and obtain a topological phase diagram for a layered quasicrystalline Weyl superconductor. To understand the difference between quasicrystalline and crystalline WSCs, we calculate the spectral density of states (SDOS) for topologically protected zero-energy modes in Sec. III B. Finally, we summarize our work in Sec IV.

II. MODEL

A. Two-dimensional quasicrystalline superconductor

We consider 2D s -wave topological superconductivity with Rashba spin-orbit coupling in an external magnetic field perpendicular to the 2D (xy) plane [54, 55] in a QC, which is modeled as [52]

$$H^{2D} = \frac{1}{2} \sum_{rr'\sigma\sigma'} (c_{r\sigma}^\dagger \ c_{r\sigma}) \begin{pmatrix} \mathcal{H}_0^{2D}(\mu) & \Delta \\ \Delta^\dagger & -\mathcal{H}_0^{2D}(\mu)^* \end{pmatrix} \begin{pmatrix} c_{r'\sigma'} \\ c_{r'\sigma'}^\dagger \end{pmatrix}, \quad (1)$$

where $c_{r\sigma}^\dagger$ is the creation operator of an electron with spin $\sigma (= \uparrow, \downarrow)$ at the r th vertex. The 2D normal-state Hamiltonian $\mathcal{H}_0^{2D}(\mu)$ is given by

$$\begin{aligned} & [\mathcal{H}_0^{2D}(\mu)]_{r\sigma, r'\sigma'} \\ &= [(t_{rr'} - \mu\delta_{rr'})\sigma_0 - h_z\delta_{rr'}\sigma_z + i\lambda_{rr'}\mathbf{e}_z \cdot \boldsymbol{\sigma} \times \hat{R}_{rr'}]_{\sigma\sigma'}, \end{aligned} \quad (2)$$

where $t_{rr'} \equiv -t$ is the hopping amplitude along nearest-neighbor links between the r th and r' th vertices, μ the chemical potential, $-h_z$ ($+h_z$) the Zeeman energy due to the external magnetic field for spin up (down), $\lambda_{rr'} \equiv \lambda$ the Rashba spin-orbit coupling constant along nearest-neighbor links between the r th and r' th vertices, \mathbf{e}_z a unit vector in the direction perpendicular to the plane, $\boldsymbol{\sigma} = (\sigma_x, \sigma_y, \sigma_z)$ the Pauli matrices acting on spin space, σ_0 an identity matrix, and $\hat{R}_{rr'}$ the normalized vector from the r th to r' th vertices. In the following, we set t as the unit of energy. An s -wave superconducting pairing operator Δ is defined as

$$[\Delta]_{r\sigma, r'\sigma'} = [\delta_{rr'} i\Delta_0 \sigma_y]_{\sigma\sigma'}, \quad (3)$$

where Δ_0 is the superconducting order parameter. In the following, we set $\lambda = 0.5t$, $h_z = -0.5t$, and $\Delta_0 = 0.2t$.

The Hamiltonian (1) describes a topological superconductor with time-reversal symmetry broken by the magnetic field, and this model belongs to class D in the Altland-Zirnbauer classification [56]. In 2D systems of class D , it is possible to define a topological invariant

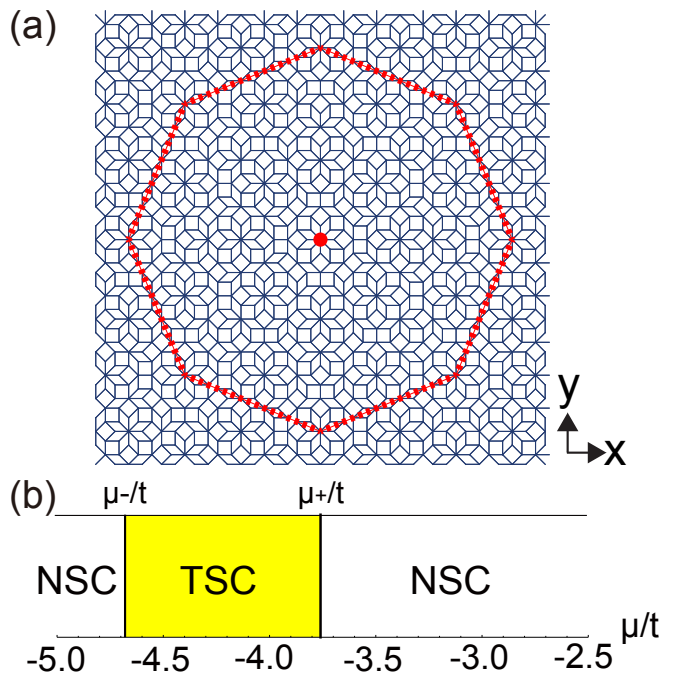


FIG. 1. (a) Ammann-Beenker approximant with 1393 vertices. The structure is identical to that of an Ammann-Beenker QC inside the octagon outlined by red dashed lines. The red circle indicates the center of the Ammann-Beenker QC. (b) Topological phase diagram as a function of chemical potential μ of the 2D model in Eq. (1) on the Ammann-Beenker QC. TSC (NSC) represents topological (normal, i.e., trivial) superconductivity with $B = 1$ ($B = 0$).

that takes on integer values. The topological invariant changes its value only when the bulk energy gap vanishes, and Majorana edge modes can appear when the invariant is nonzero in the bulk [57, 58]. Among such topological invariants, the Bott index B is applicable not only for periodic systems, but also for aperiodic systems including QCs (see Appendix A) [52, 59]. The Bott index for H^{2D} in Eq. (1) can vary as a function of μ , for example. Figure 1(a) illustrates an Ammann-Beenker approximant that contains 1393 vertices. Approximants are identical to QCs except for regions close to the edges, to which the periodic boundary condition (PBC) can be applied. In Fig. 1(a), vertices enclosed by the octagon in red dashed lines compose an Ammann-Beenker QC. Since calculation of the Bott index requires PBC imposed on the system, we use an Ammann-Beenker approximant to study the topological properties of Ammann-Beenker QCs. In Appendix B we show our study of the topological properties of Penrose QCs in terms of a Penrose approximant. Figure 1(b) is a topological phase diagram for a superconducting Ammann-Beenker QC for low electron density [52]. A topological phase transition occurs when B changes due to closing of the bulk spectral gap. In Fig. 1(b), $\mu_+/t \simeq -3.76$ and $\mu_-/t \simeq -4.68$ are the chemical potential at the topological phase boundaries [52], such that $B = 1$ for $\mu_- < \mu < \mu_+$ and $B = 0$ for μ

outside this region.

B. Layered quasicrystalline superconductor

To define quasicrystalline Weyl superconductivity, we consider periodic stacking of infinitely many, 2D quasicrystalline topological superconductors described in Sec. II A; i.e., with an external magnetic field applied in the stacking (z) direction and intralayer Rashba spin-orbit coupling. As a 2D quasicrystalline system in the xy plane, we use Ammann-Beenker QCs and apply PBC in the z direction. We introduce interlayer nearest-neighbor hopping:

$$H_z = \sum_{k_z} 2t_z \cos(k_z c) c_{k_z r \sigma}^\dagger c_{k_z r \sigma}, \quad (4)$$

where k_z and c are, respectively, momentum and the interlayer distance in the z direction, t_z is the interlayer hopping amplitude, and $c_{k_z r \sigma}^\dagger$ is the creation operator of an electron at the r th vertex in each layer with spin $\sigma (= \uparrow, \downarrow)$ and momentum k_z . Since there is an infinite number of layers, k_z is a continuous variable in the Brillouin zone, $-\pi/c \leq k_z < \pi/c$. Thus, a layered quasicrystalline superconductor is described by

$$H^{3D} = \frac{1}{2} \sum_{k_z} \sum_{r r' \sigma \sigma'} (c_{k_z r \sigma}^\dagger c_{k_z r \sigma}) \begin{pmatrix} \mathcal{H}_0^{3D}(k_z) & \Delta \\ \Delta^\dagger & -\mathcal{H}_0^{3D}(k_z)^* \end{pmatrix} \begin{pmatrix} c_{k_z r' \sigma'} \\ c_{k_z r' \sigma'}^\dagger \end{pmatrix}. \quad (5)$$

Here the 3D normal-state Hamiltonian is given by $[\mathcal{H}_0^{3D}(k_z)]_{r, r'} = [\mathcal{H}_0^{2D}(\mu)]_{r, r'} + 2t_z \cos(k_z c) \delta_{r r'} \sigma_0$, which can be written as

$$\mathcal{H}_0^{3D}(k_z) = \mathcal{H}_0^{2D}(\tilde{\mu}(k_z)) \quad (6)$$

with $\tilde{\mu}(k_z) = \mu - 2t_z \cos k_z c$. Therefore, $\tilde{\mu}(k_z)$ can be regarded as a k_z -dependent effective chemical potential in the 2D Hamiltonian.

III. RESULTS

A. Quasicrystalline Weyl nodes

We introduce a k_z -dependent Bott index $B(k_z)$ for a given k_z in RHS of Eq. (5) and define a topological invariant χ at $k_z = k_0$ as

$$\chi(k_0) = \lim_{\delta \rightarrow 0^+} [B(k_0 + \delta) - B(k_0 - \delta)]. \quad (7)$$

Nonzero $\chi(k_0)$ implies closing of the spectral gap as the Bott index changes at $k_z = k_0$. We call such a nodal point in momentum space a quasicrystalline Weyl node

[30] and define superconductivity with such Weyl nodes in QCs as quasicrystalline Weyl superconductivity.

For a given k_z , the 3D Hamiltonian of our model contains $H_0^{2D}(\tilde{\mu}(k_z))$ via Eq. (6). This means that if there is a quasicrystalline Weyl node at $k_z = k_0$, $\tilde{\mu}(k_0)$ corresponds to the chemical potential at which the 3D Hamiltonian for a given $k_z = k_0$ exhibits a topological phase transition, as illustrated in Fig. 1(b). That is,

$$\tilde{\mu}(k_0) = \mu_+ \quad \text{or} \quad \tilde{\mu}(k_0) = \mu_- \quad (8)$$

at which $B(k_0)$ changes from 1 to 0 or 0 to 1, respectively. This can occur if $|\mu - \mu_\pm| < |2t_z|$. Then, a pair of quasicrystalline Weyl nodes appears at

$$k_0 c = \pm \arccos \frac{\mu - \mu_\pm}{2t_z}. \quad (9)$$

Topological phase boundaries are given by

$$|\mu - \mu_\pm| = |2t_z|. \quad (10)$$

Figure 2(a) shows a resulting topological phase diagram. When $t_z = 0$, each layer is completely isolated with no interlayer hopping and the topological phase diagram in Fig. 2(a) reduces to Fig. 1(b). As in Fig. 1(b), the yellow region denoted as TSC in Fig. 2(a) represents a topological superconducting phase with $B(k_z) = 1$, where Majorana zero-energy modes appear at surfaces, for arbitrary k_z (for nonzero t_z). In addition, when $t_z \neq 0$ two new topological phases emerge, denoted as WSC1 (green) and WSC2 (light blue) in Fig. 2(a). The system in the WSC1 and WSC2 phase possesses, respectively, one $|k_0|$ satisfying either condition in Eq. (8) and two $|k_0|$'s satisfying their respective condition in Eq. (8). Therefore, the WSC1 (WSC2) phase is a quasicrystalline Weyl superconducting phase with a pair (two pairs) of quasicrystalline Weyl nodes. The red star (purple circle) in Fig. 2(a) indicates a representative parameter set, $\mu = \mu_+$ and $t_z = (\mu_+ - \mu_-)/4$ ($\mu = (\mu_+ + \mu_-)/2$ and $t_z = 3(\mu_+ - \mu_-)/8$), which is used for studying the WSC1 (WSC2) phase below.

We first examine the bulk band structure of our 3D model (5) calculated with PBC in all of the x , y , and z directions. The parameter set marked by the red star in Fig. 2(a) in the WSC1 phase leads to the band structure shown in Fig. 2(b), with a pair of quasicrystalline Weyl nodes at $k_0 c = \pm \pi/2$. In Fig. 2(c) $B(k_z)$ is plotted as a function of k_z , and we find $\chi = 1$ (-1) for the Weyl node at $k_0 c = -\pi/2$ ($\pi/2$). With the parameter set marked by the purple circle in Fig. 2(a) in the WSC2 phase, the band structure exhibits two pairs of quasicrystalline Weyl nodes as can be seen in Fig. 2(d). The k_z dependence of $B(k_z)$ in Fig. 2(e) shows that two nodes have $\chi = 1$ and the other two have $\chi = -1$. We note that quasicrystalline Weyl nodes with opposite signs in χ necessarily appear in pairs, so that when the system has a Weyl node with $\chi = +1$, another Weyl node with $\chi = -1$ exists.

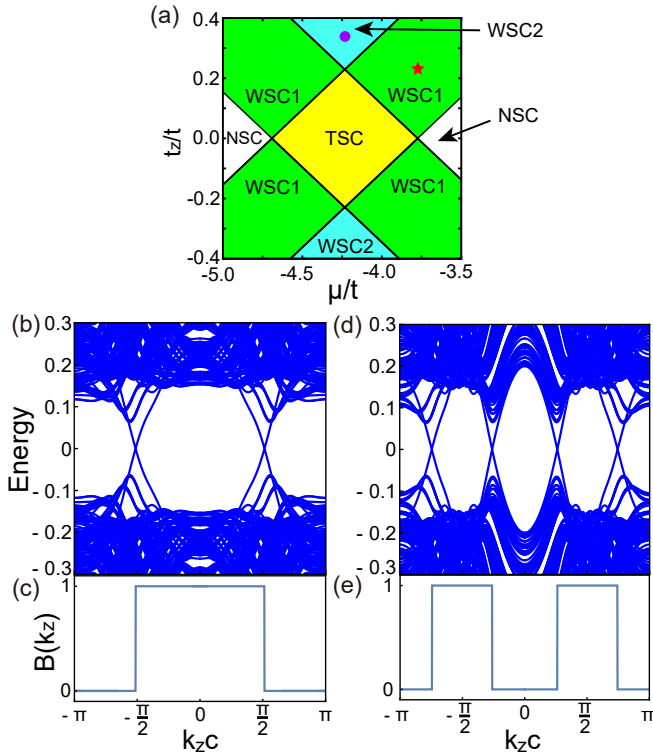


FIG. 2. (a) Topological phase diagram for a layered superconducting Ammann-Beenker QC. (b) Band structure of the model in Eq. (5) with PBC in the x , y , and z directions on layered 1393-site Ammann-Beenker approximants for the parameter set marked by the red star in (a). (c) Bott index $B(k_z)$ as a function of $k_z c$, where c is the interlayer distance, for the same system as in (b). (d) Same as (b) but for the parameter set marked by the purple circle in (a). (e) Same as (c) but for the same system as in (d).

B. Quasiperiodic Majorana arcs

It can be seen in Fig. 2(c) that $B(k_z) = 1$ for $-\pi/2 < k_z c < \pi/2$ between the two Weyl nodes, and similarly in Fig. 2(e) that $B(k_z) = 1$ between a pair of Weyl nodes for $k_z < 0$ and between another pair for $k_z > 0$. We have confirmed the existence of zero-energy Majorana surface modes for k_z between a pair of Weyl nodes where $B(k_z) \neq 0$, just as in crystalline WSCs and consistently with the bulk-boundary correspondence. We present the band structure of our system with the open boundary condition (OBC) in the x direction and PBC in the y and z directions in Fig. 3(a) (Fig. 4(a)), for the parameter set denoted by the red star (purple circle) in Fig. 2(a). Figures 3(a) and 4(a) clearly show the presence of zero-energy modes between the two Weyl nodes and each pair of Weyl nodes, respectively. These modes are Majorana surface bound states with equal-magnitude electron and hole amplitudes.

Furthermore, we calculate the spectral density of states

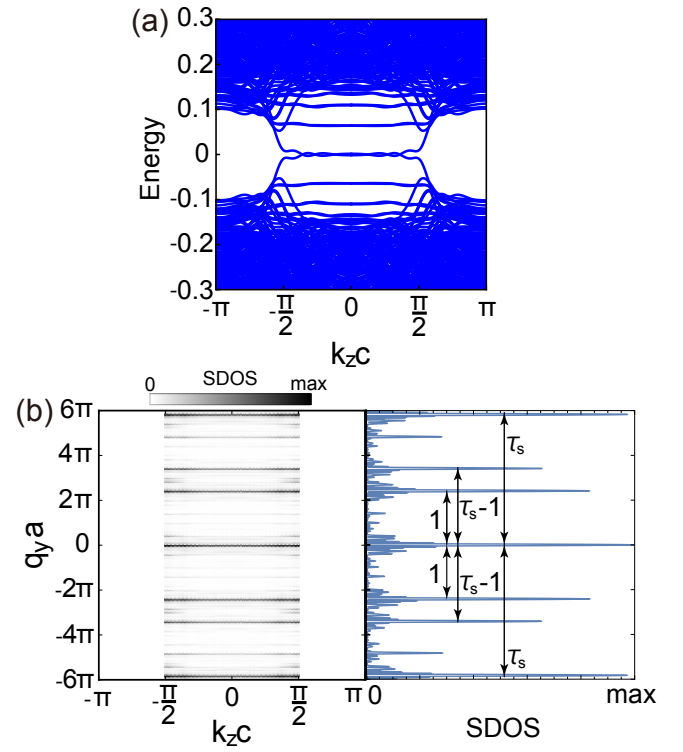


FIG. 3. (a) Band structure of the same system as in Fig. 2(b,c) but with OBC in the x direction, where zero-energy Majorana surface modes can be seen between the Weyl nodes at $k_z c = \pm\pi/2$. (b) SDOS at zero energy $\rho(q_x = 0, q_y, k_z, \varepsilon = 0)$ in the $q_y a - k_z c$ plane (left panel) and $\rho(0, q_y, k_z = 0, 0)$ as a function of $q_y a$ (right panel) for the same system as in (a). Here a is the link length in the 2D QC and the logarithm of SDOS normalized by its maximum value is shown.

(SDOS) defined as

$$\rho(q_x, q_y, k_z, \varepsilon) = \sum_{m, \sigma, \tau} |\langle q_x, q_y, k_z, \sigma, \tau | \psi_m \rangle|^2 \delta(\varepsilon - E_m), \quad (11)$$

where q_x (q_y) is Fourier momentum in the x (y) direction, ε is energy, $\tau (= e, h)$ indicates electron or hole, $|\psi_m\rangle$ and E_m are eigenstates and eigenenergies, respectively, of the 3D Bogoliubov-de-Gennes (BdG) Hamiltonian matrix in Eq. (5) with OBC in the x direction and PBC in the y and z directions. Projection onto $|q_x, q_y, k_z, \sigma, e\rangle$ ($|q_x, q_y, k_z, \sigma, h\rangle$) yields the Fourier amplitude for momentum (q_x, q_y, k_z) of the electron (hole) component of an eigenstate with spin σ . SDOS has been used to investigate the effects of band structure on superconductivity in QCs [52, 60].

The left panel in Fig. 3(b) (4(b)) shows SDOS at zero energy in the $q_y a - k_z c$ plane, $\rho(q_x = 0, q_y, k_z, \varepsilon = 0)$, where a is the link length in the 2D QC, for the parameter set marked by the red star (purple circle) in Fig. 2(a). The zero-energy SDOS is peaked at a series of $q_y a$ values, forming lines between the two (each pair of) Weyl

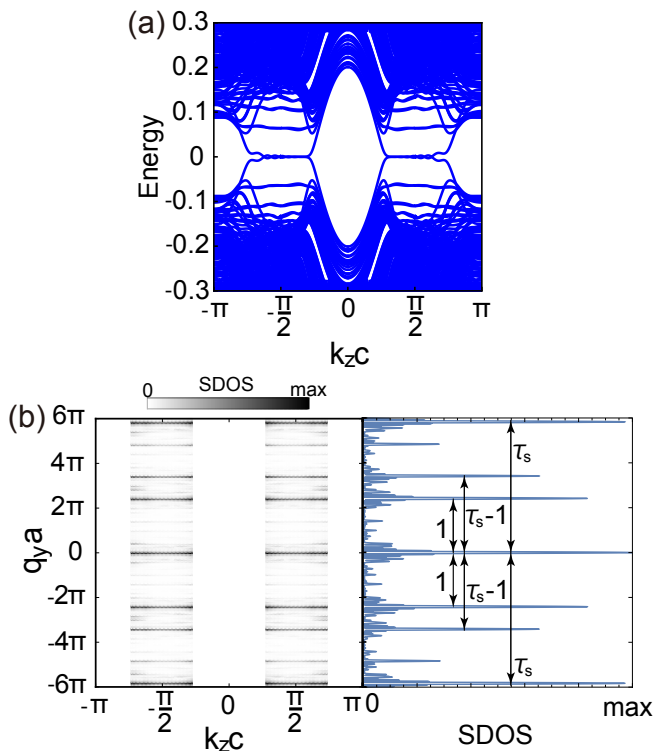


FIG. 4. (a) Same as Fig. 3(a) but for the parameter set marked by the purple circle in Fig. 2(a). Two branches of Majorana zero modes can be seen between each of the two pairs of Weyl nodes. (b) Same as Fig. 3(b) but for the same system as in (a) and zero-energy SDOS at $k_z c = \pi/2$ in the right panel.

nodes. By analogy with ‘Fermi-Bragg’ arcs in quasicrystalline Weyl semimetals [30], we call these lines Majorana arcs, which are distributed densely and quasiperiodically as a function of $q_y a$. This is illustrated in the right panels of Figs. 3(b) and 4(b), where $\rho(0, q_y, k_z = 0, 0)$ and $\rho(0, q_y, k_z c = \pi/2, 0)$, respectively, are plotted as a function of $q_y a$ and can be seen to be the largest at and symmetric about $q_y = 0$. The ratio of the smallest $|q_y a| \neq 0$ at which SDOS is substantially large (the third largest in the range shown), denoted as 1, to $|q_y a|$ for the second and fourth largest peaks in SDOS is found to be the silver ratio, $\tau_s = 1 + \sqrt{2}$, and $\tau_s - 1$, respectively. The silver ratio τ_s is associated with the structure of Ammann-Beenker QCs [61, 62]. We have checked for major peak (SDOS $> \max/2$) positions in a range much larger than shown in Figs. 3(b) and 4(b) ($|q_y a| \leq 50\pi$) that the ratio of a given $|q_y a|$ at which SDOS is peaked to another $|q_y a|$ where SDOS has another peak is given by $\alpha\tau_s + \beta$, where α and β are rational numbers. Since $\alpha\tau_s + \beta$ is an irrational number, the distribution of Majorana arcs is quasiperiodic in momentum in the direction of surfaces within each quasicrystalline layer. This makes sense, as we have also checked that the positions of major peaks in SDOS in the q_y axis match those of major Bragg peaks of Ammann-Beenker QCs. Like the Bragg peaks, with

higher resolution, an infinite number of Majorana arcs will fill in the entire q_y space.

Weyl superconductivity can also occur in periodically layered Penrose QCs. It is shown in Appendix B that Majorana arcs appear between a pair of Weyl nodes and their quasiperiodic distribution in momentum along each surface of quasicrystalline layers is characterized by the golden ratio, $\tau_g = (1 + \sqrt{5})/2$, which is inherent in the structure of Penrose QCs. The quasiperiodic distribution of Majorana arcs in quasicrystalline WSCs is in striking contrast to the periodic distribution of Majorana arcs in momentum space of crystalline WSCs. In Appendix C, we demonstrate periodic Majorana arcs in a layered square-lattice Weyl superconductor.

IV. SUMMARY

In summary, we have demonstrated the occurrence of quasicrystalline Weyl superconductivity. We have generalized the concept of Weyl superconductivity in 3D crystals to periodically stacked 2D QCs, by identifying quasicrystalline Weyl nodes in one-dimensional momentum space corresponding to the stacking direction, where the Bott index changes its value. Between two quasicrystalline Weyl nodes in momentum space, where the Bott index is nonzero, Majorana zero modes appear on surfaces. By calculating SDOS, we have found that these Majorana arcs appear densely and quasiperiodically as a function of momentum in the direction of surfaces within each 2D QC, whose quasiperiodicity is governed by the silver and golden ratio, respectively, for Ammann-Beenker and Penrose QCs.

One of the candidate materials to be a quasicrystalline WSC is a van der Waals-layered $\text{Ta}_{1.6}\text{Te}$ QC [63] whose structure consists of layered 2D dodecagonal QCs. Recently, Tokumoto *et al.* [4] have observed bulk superconductivity in $\text{Ta}_{1.6}\text{Te}$ QCs. This finding expands the possibility of realization of quasicrystalline Weyl superconductivity.

ACKNOWLEDGMENTS

We thank Yuki Tokumoto for useful discussions. This work was supported by JSPS KAKENHI (Grant No. 23K13033), JST SPRING (Grant No. JPMJSP2151), and the Natural Sciences and Engineering Research Council of Canada.

Appendix A: Bott index

We review the Bott index B [59] which is an integer topological invariant. Whether the system is periodic or not, the Bott index B topologically classifies phases of a 2D system whose Hamiltonian belongs to class D , including time-reversal-breaking superconductors [52, 56–

59]. In a superconducting state with $B \neq 0$, Majorana zero-energy modes can appear at surfaces or topological defects.

The Bott index is given by

$$B = \frac{1}{2\pi} \text{ImTr}[\log(U_Y U_X U_Y^\dagger U_X^\dagger)], \quad (\text{A1})$$

where U_X (U_Y) is a projected position operator in the x (y) direction. Using an occupation projector that is defined as

$$P = \sum_{E_m < 0} |\psi_m\rangle \langle \psi_m|, \quad (\text{A2})$$

the projected position operators are given by

$$U_X = P e^{2\pi i X} P + (I - P), \quad U_Y = P e^{2\pi i Y} P + (I - P), \quad (\text{A3})$$

where $|\psi_m\rangle$ is an eigenstate of the Bogoliubov-de-Gennes Hamiltonian for a given system with a negative eigenvalue E_m , X (Y) is a rescaled position operator defined in the interval $[0, 1]$ in the x (y) direction, and I is an identity operator. When the spectral gap of the system closes as a system parameter is varied, the value of B can change. In the thermodynamic limit, any 2D system with OBC has $B = 0$. Therefore, we use approximants of Ammann-Beenker and Penrose QCs with PBC in both directions to calculate B .

Appendix B: Quasicrystalline Weyl superconductivity in layered Penrose QCs

We consider periodically stacked, superconducting Penrose QCs whose Hamiltonian is given by Eq. (5). For Penrose QCs, by using $\mu_+/t \simeq -3.77$ and $\mu_-/t \simeq -4.69$ [52], we obtain a topological phase diagram similar to Fig. 2(a). We choose two parameter sets given by $\mu = \mu_+$ and $t_z = (\mu_+ - \mu_-)/4$, and $\mu = (\mu_+ + \mu_-)/2$ and $t_z = 3(\mu_+ - \mu_-)/8$, to calculate the band structure which is shown in Figs. 5(a) and 5(b), respectively. Figure 5(a) (5(b)) shows the band structure of the model with PBC in the x , y , and z directions, where we find a pair (two pairs) of quasicrystalline Weyl nodes. It can be seen from the Bott index $B(k_z)$ shown in Figs. 5(c) and 5(d) that $\chi = +1$ or -1 at each of these Weyl nodes.

Figure 6(a) (7(a)) shows the band structure of the model with OBC in the x direction and PBC in the y and z directions for the first (second) parameter set above. Zero-energy modes appear at surfaces between two quasicrystalline Weyl nodes in k_z space, where the Bott index is nonzero. We have calculated SDOS in Eq. (11) and present $\rho(q_x = 0, q_y, k_z, \varepsilon = 0)$ in the left panel of Fig. 6(b) (7(b)), where Majorana arcs can be seen between the two (each pair of) Weyl nodes at densely and quasiperiodically distributed positions in $q_y a$. This is illustrated further in terms of $\rho(0, q_y, k_z = 0, 0)$ and $\rho(0, q_y, k_z = \pi/2, 0)$ shown in the right panels

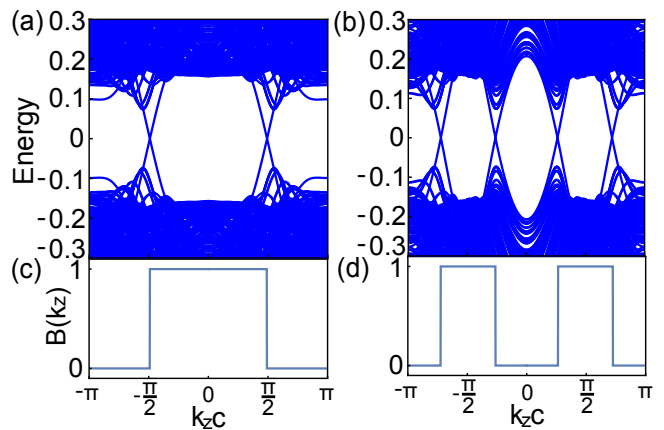


FIG. 5. (a) Band structure of the model in Eq. (5) for layered 3571-site Penrose approximants with PBC in the x , y , and z directions, for $\mu = \mu_+$ and $t_z = (\mu_+ - \mu_-)/4$. (b) Same as (a) but for $\mu = (\mu_+ + \mu_-)/2$ and $t_z = 3(\mu_+ - \mu_-)/8$. (c) The Bott index $B(k_z)$ as a function of $k_z c$ for the same system as in (a). (d) Same as (c) but for the same system as in (b).

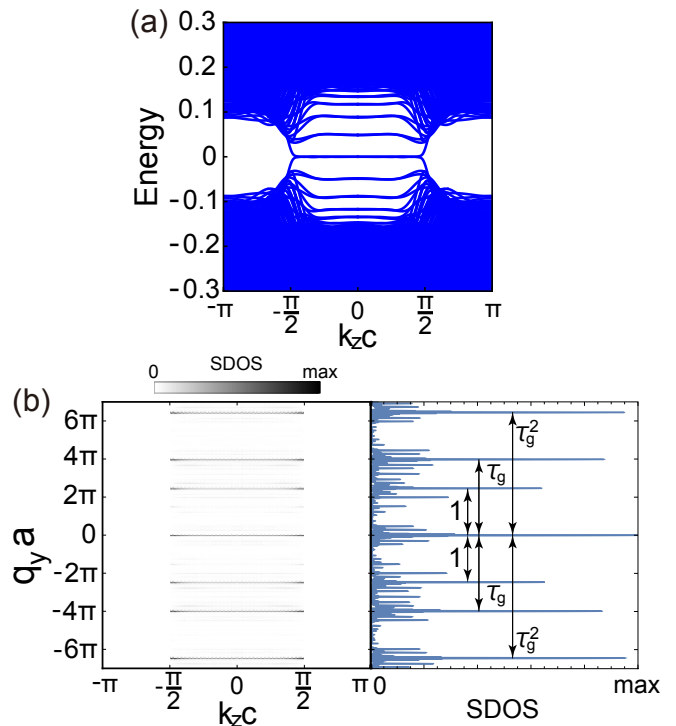


FIG. 6. (a) Band structure of the same system as in Fig. 5(a,c) but with OBC in the x direction, showing Majorana surface states between the two Weyl nodes at $k_z c = \pm\pi/2$. (b) Logarithm of SDOS at zero energy $\rho(q_x = 0, q_y, k_z, \varepsilon = 0)$ in the $q_y a$ - $k_z c$ plane (left panel) and $\rho(0, q_y, k_z = 0, 0)$ as a function of $q_y a$ (right panel), where a is the link length in the 2D QC, for the same system as in (a).

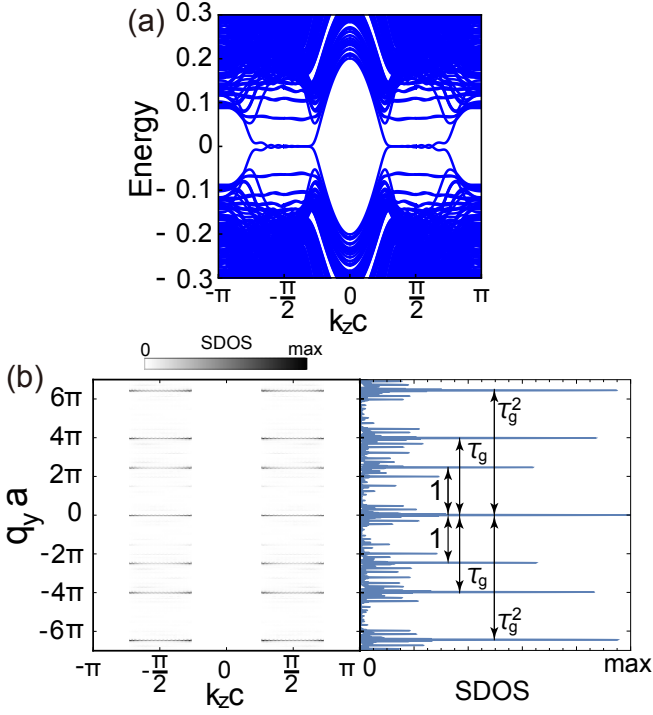


FIG. 7. (a) Same as Fig. 6(a) but for $\mu = (\mu_+ + \mu_-)/2$ and $t_z = 3(\mu_+ - \mu_-)/8$, where Majorana zero modes appear between each pair of Weyl nodes. (b) Same as Fig. 6(b) but for the same system as in (a) and zero-energy SDOS at $k_z c = \pi/2$ in the right panel.

of Figs. 6(b) and 7(b), respectively. As in Ammann-Beenker QCs, SDOS is the largest at and symmetric about $q_y = 0$. The ratio of the smallest $|q_y a| \neq 0$ at which SDOS has a major peak (the fourth highest in the range shown) to $|q_y a|$ for the third and second highest peaks is found to be, respectively, $1 : \tau_g$ and $1 : \tau_g^2$, where $\tau_g = (1 + \sqrt{5})/2$ is the golden ratio. Geometric and physical properties of Penrose QCs are governed by τ_g [61, 64, 65]. We have confirmed for $|q_y a| \leq 50\pi$ that the ratio of $|q_y a|$ for a major peak (SDOS $> \max/2$) in SDOS to $|q_y a|$ for another major peak can be expressed as $1 : \alpha\tau_g + \beta$, where α and β are rational numbers, and that those peak positions coincide with $q_y a$ values of major Bragg peaks of Penrose QCs. Hence, similarly to Ammann-Beenker QCs, layered Penrose QCs exhibit quasicrystalline Weyl superconductivity, with Majorana arcs between a pair of quasicrystalline Weyl nodes positioned quasiperiodically in momentum in the direction of surfaces within each layer.

Appendix C: Comparison with a crystalline WSC

We now study a layered square-lattice superconductor whose Hamiltonian is given by Eq. (5). For a square

lattice, topological phase boundaries are given analytically by $\mu_{\pm} = -4t \pm \sqrt{h_z^2 - \Delta_0^2}$ in the low-filling limit

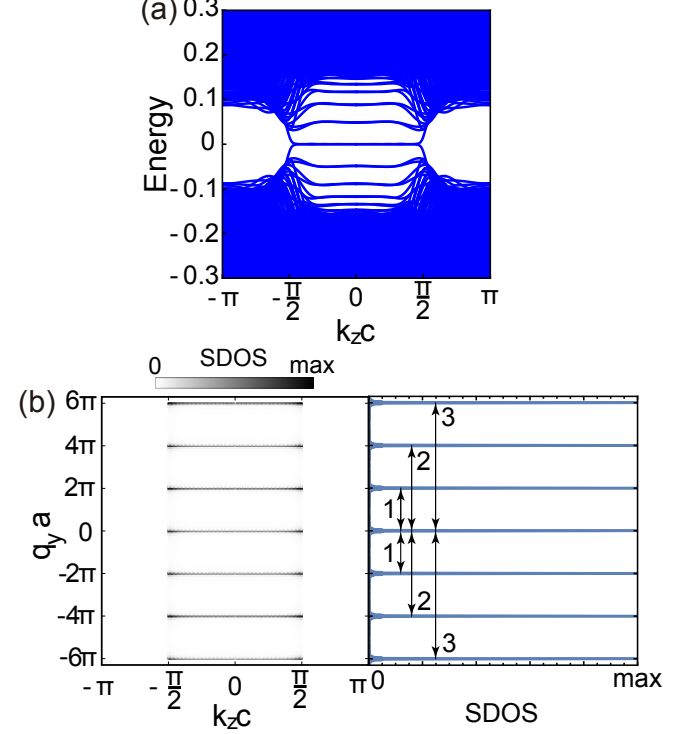


FIG. 8. (a) Band structure of a layered square-lattice Weyl superconductor with OBC in the x direction and PBC in the y and z directions, for $\mu = \mu_+$ and $t_z = (\mu_+ - \mu_-)/4$. (b) Logarithm of SDOS at zero energy $\rho(q_x = 0, q_y, k_z, \varepsilon = 0)$ in the $q_y a - k_z c$ plane (left panel) and $\rho(0, q_y, k_z = 0, 0)$ as a function of $q_y a$ (right panel) for the system as in (a), where a is the lattice constant of the square lattice. Each layer has 50×50 lattice sites.

[54, 55], which yield a topological phase diagram similar to Fig. 2(a). For the parameter set $\mu = \mu_+$ and $t_z = (\mu_+ - \mu_-)/4$, the band structure shows one pair of Weyl nodes with $\chi = \pm 1$ (at $k_z c = \mp\pi/2$), which is chirality of each Weyl node in this case. The band structure of the model with OBC in the x direction and PBC in the y and z directions is presented in Fig. 8(a), where zero-energy surface states can be seen. The corresponding SDOS $\rho(q_x = 0, q_y, k_z, \varepsilon = 0)$ is shown in the left panel of Fig. 8(b), where Majorana arcs appear between the two Weyl nodes where the Bott index is unity. As illustrated in the right panel of Fig. 8(b) in terms of $\rho(0, q_y, k_z = 0, 0)$, the Majorana arcs are equally spaced in q_y and positioned at $q_y a = 0, \pm 2\pi, \pm 4\pi, \pm 6\pi, \dots$. Therefore, any distance from a given Majorana arc to another Majorana arc is a natural number multiple of 2π and their ratio is a rational number, as indicated in the right panel of Fig. 8(b). This contrasts with the quasiperiodic distribution of Majorana arcs in quasicrystalline WSCs, where an irrational number characterizes those ratios.

-
- [1] D. Shechtman, I. Blech, D. Gratias, and J. W. Cahn, Metallic phase with long-range orientational order and no translational symmetry, *Phys. Rev. Lett.* **53**, 1951 (1984).
- [2] R. Tamura, A. Ishikawa, S. Suzuki, T. Kotajima, Y. Tanaka, T. Seki, N. Shibata, T. Yamada, T. Fujii, C.-W. Wang, M. Avdeev, K. Nawa, D. Okuyama, and T. J. Sato, Experimental observation of long-range magnetic order in icosahedral quasicrystals, *J. Am. Chem. Soc.* **143**, 19938 (2021).
- [3] K. Kamiya, T. Takeuchi, N. Kabeya, N. Wada, T. Ishimasa, A. Ochiai, K. Deguchi, K. Imura, and N. K. Sato, Discovery of superconductivity in quasicrystal, *Nat. Commun.* **9**, 154 (2018).
- [4] Y. Tokumoto, K. Hamano, S. Nakagawa, Y. Kamimura, S. Suzuki, R. Tamura, and K. Edagawa, Superconductivity in a van der Waals layered quasicrystal, arXiv:2307.10679.
- [5] S. Sakai, N. Takemori, A. Koga, and R. Arita, Superconductivity on a quasiperiodic lattice: Extended-to-localized crossover of Cooper pairs, *Phys. Rev. B* **95**, 024509 (2017).
- [6] S. Sakai and R. Arita, Exotic pairing state in quasicrystalline superconductors under a magnetic field, *Phys. Rev. Res.* **1**, 022002(R) (2019).
- [7] N. Takemori, R. Arita, and S. Sakai, Physical properties of weak-coupling quasiperiodic superconductors, *Phys. Rev. B* **102**, 115108 (2020).
- [8] T. Fukushima, N. Takemori, S. Sakai, M. Ichioka, and A. Jagannathan, Supercurrent distribution on Ammann-Beenker structure, *J. Phys.: Conf. Ser.* **2461**, 012014 (2023).
- [9] T. Fukushima, N. Takemori, S. Sakai, M. Ichioka, and A. Jagannathan, Supercurrent distribution in real-space and anomalous paramagnetic response in a superconducting quasicrystal, *Phys. Rev. Res.* **5**, 043164 (2023).
- [10] J. Fan and H. Huang, Topological states in quasicrystals, *Front. Phys.* **17**, 13203 (2021).
- [11] D.-T. Tran, A. Dauphin, N. Goldman, and P. Gaspard, Topological Hofstadter insulators in a two-dimensional quasicrystal, *Phys. Rev. B* **91**, 085125 (2015).
- [12] M. A. Bandres, M. C. Rechtsman, and M. Segev, Topological photonic quasicrystals: Fractal topological spectrum and protected transport, *Phys. Rev. X* **6**, 011016 (2016).
- [13] H. Huang and F. Liu, Theory of spin Bott index for quantum spin Hall states in nonperiodic systems, *Phys. Rev. B* **98**, 125130 (2018).
- [14] H. Huang and F. Liu, Quantum spin Hall effect and spin Bott index in a quasicrystal lattice, *Phys. Rev. Lett.* **121**, 126401 (2018).
- [15] H. Huang and F. Liu, Comparison of quantum spin Hall states in quasicrystals and crystals, *Phys. Rev. B* **100**, 085119 (2019).
- [16] A.-L. He, L.-R. Ding, Y. Zhou, Y.-F. Wang, and C.-D. Gong, Quasicrystalline Chern insulators, *Phys. Rev. B* **100**, 214109 (2019).
- [17] D. Varjas, A. Lau, K. Pöyhönen, A. R. Akhmerov, D. I. Pikulin, and I. C. Fulga, Topological phases without crystalline counterparts, *Phys. Rev. Lett.* **123**, 196401 (2019).
- [18] R. Chen, C.-Z. Chen, J.-H. Gao, B. Zhou, and D.-H. Xu, Higher-order topological insulators in quasicrystals, *Phys. Rev. Lett.* **124**, 036803 (2020).
- [19] C. W. Duncan, S. Manna, and A. E. B. Nielsen, Topological models in rotationally symmetric quasicrystals, *Phys. Rev. B* **101**, 115413 (2020).
- [20] C.-B. Hua, R. Chen, B. Zhou, and D.-H. Xu, Higher-order topological insulator in a dodecagonal quasicrystal, *Phys. Rev. B* **102**, 241102(R) (2020).
- [21] Y. E. Kraus, Y. Lahini, Z. Ringel, M. Verbin, and O. Zeitlinger, Topological states and adiabatic pumping in quasicrystals, *Phys. Rev. Lett.* **109**, 106402 (2012).
- [22] S. Nakajima, N. Takei, K. Sakuma, Y. Kuno, P. Marra, and Y. Takahashi, Competition and interplay between topology and quasi-periodic disorder in Thouless pumping of ultracold atoms, *Nat. Phys.* **17**, 844 (2021).
- [23] M. Yoshii, S. Kitamura, and T. Morimoto, Topological charge pumping in quasiperiodic systems characterized by the Bott index, *Phys. Rev. B* **104**, 155126 (2021).
- [24] M. Koshino and H. Oka, Topological invariants in two-dimensional quasicrystals, *Phys. Rev. Res.* **4**, 013028 (2022).
- [25] K. Yamamoto and M. Koshino, Topological gap labeling with third Chern numbers in three-dimensional quasicrystals, *Phys. Rev. B* **105**, 115410 (2022).
- [26] T. Timusk, J. P. Carbotte, C. C. Homes, D. N. Basov, and S. G. Sharapov, Three-dimensional Dirac fermions in quasicrystals as seen via optical conductivity, *Phys. Rev. B* **87**, 235121 (2013).
- [27] J. H. Pixley, J. H. Wilson, D. A. Huse, and S. Gopalakrishnan, Weyl semimetal to metal phase transitions driven by quasiperiodic potentials, *Phys. Rev. Lett.* **120**, 207604 (2018).
- [28] V. Mastropietro, Stability of Weyl semimetals with quasiperiodic disorder, *Phys. Rev. B* **102**, 045101 (2020).
- [29] J. D. Cain, A. Azizi, M. Conrad, S. M. Griffin, and A. Zettl, Layer-dependent topological phase in a two-dimensional quasicrystal and approximant, *Proc. Natl. Acad. Sci. USA* **117**, 26135 (2020).
- [30] A. Grossi e Fonseca, T. Christensen, J. D. Joannopoulos, and M. Soljačić, Quasicrystalline Weyl points and dense Fermi-Bragg arcs, *Phys. Rev. B* **108**, L121109 (2023).
- [31] Y.-F. Mao, Y.-L. Tao, J.-H. Wang, Q.-B. Zeng, and Y. Xu, Higher-order topological insulators and semimetals in three dimensions without crystalline counterparts, arXiv preprint arXiv:2307.14974.
- [32] R. Chen, B. Zhou, and D.-H. Xu, Quasicrystalline second-order topological semimetals, *Phys. Rev. B* **108**, 195306 (2023).
- [33] T. Meng and L. Balents, Weyl superconductors, *Phys. Rev. B* **86**, 054504 (2012).
- [34] J. D. Sau and S. Tewari, Topologically protected surface Majorana arcs and bulk Weyl fermions in ferromagnetic superconductors, *Phys. Rev. B* **86**, 104509 (2012).
- [35] M. H. Fischer, T. Neupert, C. Platt, A. P. Schnyder, W. Hanke, J. Goryo, R. Thomale, and M. Sigrist, Chiral *d*-wave superconductivity in SrPtAs, *Phys. Rev. B* **89**, 020509(R) (2014).
- [36] S. A. Yang, H. Pan, and F. Zhang, Dirac and Weyl superconductors in three dimensions, *Phys. Rev. Lett.* **113**, 046401 (2014).

- [37] G. Bednik, A. A. Zyuzin, and A. A. Burkov, Superconductivity in Weyl metals, *Phys. Rev. B* **92**, 035153 (2015).
- [38] N. F. Q. Yuan, W.-Y. He, and K. T. Law, Superconductivity-induced ferromagnetism and Weyl superconductivity in Nb-doped Bi_2Se_3 , *Phys. Rev. B* **95**, 201109(R) (2017).
- [39] Y. Li and F. D. M. Haldane, Topological nodal Cooper pairing in doped Weyl metals, *Phys. Rev. Lett.* **120**, 067003 (2018).
- [40] R. Okugawa and T. Yokoyama, Generic phase diagram for Weyl superconductivity in mirror-symmetric superconductors, *Phys. Rev. B* **97**, 060504(R) (2018).
- [41] S. Sumita and Y. Yanase, Unconventional superconducting gap structure protected by space group symmetry, *Phys. Rev. B* **97**, 134512 (2018).
- [42] R. Nakai and K. Nomura, Weyl superconductor phases in a Weyl-semimetal/superconductor multilayer, *Phys. Rev. B* **101**, 094510 (2020).
- [43] X. Wan, A. M. Turner, A. Vishwanath, and S. Y. Savrasov, Topological semimetal and Fermi-arc surface states in the electronic structure of pyrochlore iridates, *Phys. Rev. B* **83**, 205101 (2011).
- [44] A. A. Burkov and L. Balents, Weyl semimetal in a topological insulator multilayer, *Phys. Rev. Lett.* **107**, 127205 (2011).
- [45] R. Okugawa and S. Murakami, Dispersion of Fermi arcs in Weyl semimetals and their evolutions to Dirac cones, *Phys. Rev. B* **89**, 235315 (2014).
- [46] A. P. Schnyder and P. M. R. Brydon, Topological surface states in nodal superconductors, *J. Phys.: Condense. Matter* **27**, 243201 (2015).
- [47] N. Read and D. Green, Paired states of fermions in two dimensions with breaking of parity and time-reversal symmetries and the fractional quantum Hall effect, *Phys. Rev. B* **61**, 10267 (2000).
- [48] I. C. Fulga, D. I. Pikulin, and T. A. Loring, Aperiodic weak topological superconductors, *Phys. Rev. Lett.* **116**, 257002 (2016).
- [49] Y. Cao, Y. Zhang, Y.-B. Liu, C.-C. Liu, W.-Q. Chen, and F. Yang, Kohn-Luttinger mechanism driven exotic topological superconductivity on the Penrose lattice, *Phys. Rev. Lett.* **125**, 017002 (2020).
- [50] C. Wang, F. Liu, and H. Huang, Effective model for fractional topological corner modes in quasicrystals, *Phys. Rev. Lett.* **129**, 056403 (2022).
- [51] Y.-B. Liu, Y. Zhang, W.-Q. Chen, and F. Yang, High-angular-momentum topological superconductivities in twisted bilayer quasicrystal systems, *Phys. Rev. B* **107**, 014501 (2023).
- [52] R. Ghadimi, T. Sugimoto, K. Tanaka, and T. Tohyama, Topological superconductivity in quasicrystals, *Phys. Rev. B* **104**, 144511 (2021).
- [53] M. Hori, T. Sugimoto, T. Tohyama, and K. Tanaka, Self-consistent study of topological superconductivity in two-dimensional quasicrystals, arXiv preprint arXiv:2401.06355 .
- [54] M. Sato, Y. Takahashi, and S. Fujimoto, Non-Abelian topological order in *s*-wave superfluids of ultracold fermionic atoms, *Phys. Rev. Lett.* **103**, 020401 (2009).
- [55] M. Sato, Y. Takahashi, and S. Fujimoto, Non-Abelian topological orders and Majorana fermions in spin-singlet superconductors, *Phys. Rev. B* **82**, 134521 (2010).
- [56] A. Altland and M. R. Zirnbauer, Nonstandard symmetry classes in mesoscopic normal-superconducting hybrid structures, *Phys. Rev. B* **55**, 1142 (1997).
- [57] A. P. Schnyder, S. Ryu, A. Furusaki, and A. W. W. Ludwig, Classification of topological insulators and superconductors in three spatial dimensions, *Phys. Rev. B* **78**, 195125 (2008).
- [58] C.-K. Chiu, J. C. Y. Teo, A. P. Schnyder, and S. Ryu, Classification of topological quantum matter with symmetries, *Rev. Mod. Phys.* **88**, 035005 (2016).
- [59] T. A. Loring and M. B. Hastings, Disordered topological insulators via C^* -algebras, *Europhys. Lett.* **92**, 67004 (2011).
- [60] R. N. Araújo and E. C. Andrade, Conventional superconductivity in quasicrystals, *Phys. Rev. B* **100**, 014510 (2019).
- [61] C. Janot, *Quasicrystals - A Primer* (Carendon Press, Oxford, 1992).
- [62] A. Koga, Superlattice structure in the antiferromagnetically ordered state in the Hubbard model on the Ammann-Beenker tiling, *Phys. Rev. B* **102**, 115125 (2020).
- [63] M. Conrad, F. Krumeich, and B. Harbrecht, A dodecagonal quasicrystalline chalcogenide, *Angew. Chem. Int. Ed.* **37**, 1383 (1998).
- [64] J.-M. Gambaudo and P. Vignolo, Brillouin zone labelling for quasicrystals, *New J. Phys.* **16**, 043013 (2014).
- [65] A. Koga and H. Tsunetsugu, Antiferromagnetic order in the Hubbard model on the Penrose lattice, *Phys. Rev. B* **96**, 214402 (2017).